



DØNote 6342-CONF

Updated search for $ZH \rightarrow \ell^+ \ell^- b\bar{b}$ production in 9.7 fb^{-1} of $p\bar{p}$ collisions

The DØ Collaboration

URL <http://www-d0.fnal.gov>

Dated July 1, 2012

We present an update of a search for a standard model (SM) Higgs boson produced in association with a Z boson in 9.7 fb^{-1} of $p\bar{p}$ collisions, collected with the DØ detector at the Fermilab Tevatron at $\sqrt{s} = 1.96 \text{ TeV}$. Selected events contain one reconstructed $Z \rightarrow e^+e^-$ or $Z \rightarrow \mu^+\mu^-$ candidate and at least two jets, including at least one b -tagged jet. The data are consistent with the background expected from other SM processes. Upper limits at 95% C.L. on the ZH production cross section times branching ratio for $H \rightarrow b\bar{b}$ are set for Higgs boson masses $90 < M_H < 150 \text{ GeV}$. The observed (expected) limit for $M_H = 115 \text{ GeV}$ is a factor of 4.3 (3.7) larger than the SM prediction. At $M_H = 125 \text{ GeV}$ it is a factor of 7.1 (5.1) larger than the SM prediction.

Preliminary Results for ICHEP'12

I. INTRODUCTION

In the standard model (SM), the spontaneous breakdown of the electroweak gauge symmetry generates masses for the W and Z bosons and produces a residual massive particle, the Higgs boson, which has so far eluded detection. The discovery of the Higgs boson would be an essential confirmation of SM prediction. The combination of constraints from direct searches at LEP [1] and from precision electroweak observables [2] result in a preferred range for the Higgs boson mass of $114.4 < M_H < 152$ GeV at 95% C.L. Direct searches at CDF and DØ [3], and at the LHC [4, 5] further restrict the allowed range to $122 < M_H < 127$ GeV. For Higgs boson masses $M_H \lesssim 135$ GeV, the primary decay is to $b\bar{b}$. At a hadron collider, the gluon-gluon fusion production mechanism with this final state has copious background. Consequently, the best sensitivity to a low-mass Higgs boson is obtained from the analysis of its production in association with a W or Z boson.

We present a search for $ZH \rightarrow \ell^+\ell^-b\bar{b}$, where ℓ is either a muon or an electron. The search for $ZH \rightarrow \nu\bar{\nu}b\bar{b}$ is treated elsewhere [6]. The data for this analysis were collected at the Fermilab Tevatron $p\bar{p}$ Collider with $\sqrt{s} = 1.96$ TeV, with the D0 detector [7] from April 2002 to February 2006 (Run IIa), and from June 2006 to September 2011 (Run IIb). It corresponds to the full dataset with an integrated luminosity of 9.7 fb^{-1} after data quality requirements were invoked. Between Run IIa and Run IIb, a new layer of the silicon microstrip tracker was installed, and the trigger system was upgraded [8]. The analyzed events were acquired predominantly with triggers that select electron and muon candidates. However, events satisfying any trigger requirement are considered in this analysis.

This note documents an update to a previous search of the same final states and with the same integrated luminosity [9]. The most notable change is that we introduce a new strategy of the multivariate analysis as described in Section V. We now train a dedicated discriminant against $t\bar{t}$ events and use it to define $t\bar{t}$ enriched and $t\bar{t}$ depleted regions. We train separate discriminants in each of these regions that are used as the final variables to extract results. Thanks to this new strategy, we have reduced the expected upper limit on the cross section to 0.86 of its previous value. In addition, we have made several changes to our selection requirements. We have adopted a more stringent dilepton mass requirement; removed criteria on the missing transverse energy and on the opening angle in azimuth between the dilepton and dijet system; and applied additional track matching requirements for reconstructed jets. We also extend the analysis to include results for Higgs boson masses of 90 and 95 GeV.

II. DØ DETECTOR

The detector consists of a central tracking system in a 2 T superconducting solenoidal magnet, surrounded by a central preshower (CPS) detector, a liquid-argon sampling calorimeter, and a muon system. The central tracking system, consisting of a silicon microstrip tracker (SMT) and a scintillating fiber tracker (CFT), provides coverage for charged particles in the pseudorapidity range $|\eta_{\text{det}}| < 3$ [10]. The CPS is located immediately before the inner layer of the calorimeter, and has about one radiation length of absorber, followed by three layers of scintillating strips. The calorimeter consists of a central calorimeter (CC) with coverage of $|\eta_{\text{det}}| < 1.1$, and two endcap calorimeters (EC) covering up to $|\eta_{\text{det}}| \approx 4.2$. The calorimeters are sub-divided into electromagnetic (EM) layers on the inside and hadronic layers on the outside. Between the CC and EC, plastic scintillator detectors (ICD) enhance the calorimeter coverage. The muon system resides beyond the calorimeter and consists of a layer of tracking detectors and scintillation trigger counters before a 1.8 T iron toroidal magnet, followed by two similar layers after the toroid. The muon system provides coverage up to $|\eta_{\text{det}}| < 2$. The instantaneous luminosity is measured by a system composed of two arrays of scintillating tile detectors positioned in front of the EC's. Finally, a three-level trigger system provides event selection. More details on the detector can be obtained in Refs. [7] and [8].

III. EVENT SELECTION

The event selection requires a primary $p\bar{p}$ interaction vertex (PV) that has at least three associated tracks, and is located within ± 60 cm of the center of the detector along the beam direction. Selected events must contain a $Z \rightarrow \ell^+\ell^-$ candidate with a dilepton invariant mass $70 < m_{\ell\ell} < 110$ GeV. The analysis is conducted in four separate channels organized by the reconstruction of the $Z \rightarrow \ell^+\ell^-$ candidate in the detector. The dimuon and dielectron channels include events with two fully reconstructed muons or electrons from the Z boson decay. In addition, the muon-plus-track ($\mu\mu_{\text{trk}}$) and electron-plus-ICR (ee_{ICR}) channels are designed to recover events in which one of the leptons goes into a poorly-instrumented region of the detector.

The dimuon ($\mu\mu$) selection requires at least two muons identified in the muon system, matched to central tracks (referred to as combined muons) with transverse momenta $p_T > 10$ GeV. Each muon-associated track must satisfy $|\eta_{\text{det}}| < 2$. At least one muon must have $|\eta_{\text{det}}| < 1.5$ and $p_T > 15$ GeV. The distance between the PV and each

muon-associated track along the z axis, d_{PV}^z must be less than 1 cm. The distance of closest approach of each muon-associated track to the PV in the plane transverse to the beam direction, d_{PV} , must be less than 0.04 cm for tracks with at least one hit in the SMT. A track without any SMT hits must have $d_{PV} < 0.2$ cm, and its p_T is corrected through a constraint to the position of the PV. The muons should be isolated from jets, from other tracks and from energy deposited in the calorimeter. At least one of the muons must be separated from any jet with $p_T > 20$ GeV and $|\eta_{\text{det}}| < 2.5$ by $\Delta\mathcal{R} = \sqrt{\Delta\eta^2 + \Delta\phi^2} > 0.5$. If only one muon satisfies this criterion, it must be also isolated in the tracker and calorimeter. If both muons satisfy the requirement on $\Delta\mathcal{R}$ then the leading muon must satisfy track and calorimeter isolation. To reduce contamination from cosmic rays, the muon-associated tracks must not be back-to-back in η and ϕ . The two muon-associated tracks must also have opposite charge.

The $\mu\mu_{\text{trk}}$ selection is designed to recover dimuon events in which one muon is not identified in the muon system. This selection requires exactly one combined muon with $|\eta_{\text{det}}| < 1.5$ and $p_T > 15$ GeV which has to be isolated both in the tracker and in the calorimeter. To ensure that the $\mu\mu$ and $\mu\mu_{\text{trk}}$ selections do not overlap, events containing any additional combined muons with $|\eta_{\text{det}}| < 2$ and $p_T > 10$ GeV are rejected. In addition, a track reconstructed in the SMT and CFT with $|\eta_{\text{det}}| < 2$ and $p_T > 20$ GeV must be present. This track-only muon is only reconstructed in the central tracking system, and is required to have at least one SMT hit and at least two CFT hits. The track must have $d_{PV} < 0.02$ cm and $d_{PV}^z < 1$ cm. It is also required to be isolated in the tracker. Its distance $\Delta\mathcal{R}$ from the combined muon and from any jet of $p_T > 15$ GeV and $|\eta_{\text{det}}| < 2.5$ must be greater than 0.1 and 0.5, respectively. The combined muon and track-only muon must have opposite charges. For the very small fraction of events with more than one track passing these requirements, the track whose invariant mass with the combined muon is closest to the Z boson mass is chosen.

The dielectron (ee) selection requires at least two electrons with $p_T > 15$ GeV that pass selection requirements based on the energy deposition and shower shape in the calorimeter and the CPS. The two electrons are required to be isolated in both the tracker and the calorimeter. At least one electron must be identified in the CC, and a second electron either in the CC or in the EC. The CC electrons must match central tracks or a set of hits in the tracker consistent with that of an electron trajectory.

The ee_{ICR} selection requires exactly one electron in either the CC or EC with $p_T > 15$ GeV, and an “ICR track” pointing toward one of the inter-cryostat regions of the calorimeter, $1.1 < |\eta_{\text{det}}| < 1.5$, where the electromagnetic calorimeter coverage is limited. The ICR track must be isolated and matched to a calorimeter energy deposit with $E_T > 15$ GeV. When the electron is found in the EC, the ICR electron candidate is required to be in the adjoining inter-cryostat region. The background from multijet events is suppressed by applying a requirement on a multivariate discriminant originally designed to identify τ candidates.

Jets are reconstructed in the calorimeter using the iterative midpoint cone algorithm [11] with a cone of radius 0.5 in the plane of rapidity and azimuth. The energy scale of jets is corrected for detector response, noise and multiple interactions, and energy deposited outside of the reconstructed jet cone. At least two jets with $p_T > 20$ GeV and $|\eta_{\text{det}}| < 2.5$ are required. For the ee and ee_{ICR} selections, jets must be separated from an electron by $\Delta\mathcal{R} > 0.5$. To reduce the impact from multiple interactions at high instantaneous luminosities, jets must be associated with tracks originating from the PV that satisfy minimal quality requirements. The dimuon and dielectron mass spectra, after requiring two leptons and at least two jets are shown in Fig. 1. In this Figure, and others throughout this note, the ZH signal shown is for $M_H = 125$ GeV. The invariant mass of the dijet system (constructed from the two jets with the highest p_T) in the combination of all selections is shown in Fig 2. In this note, we use “inclusive” to denote the events selected just by requiring the presence of two leptons, and use “pretag” for the events which meet the additional requirement of having at least two jets.

To distinguish events containing a $H \rightarrow b\bar{b}$ decay from background processes involving light quarks and gluons, jets are identified as likely to contain b -quarks (b -tagged) if they pass “loose” or “tight” requirements on the output of a multivariate discriminant trained to separate b -jets from light jets. This discriminant is an improved version of the neural network b -tagging discriminant described in Ref. [12]. For $|\eta| < 1.1$ and $p_T \approx 50$ GeV, the b -tagging efficiency for b -jets and the misidentification rate of light jets are, respectively, 72% and 6.7% for loose b -tags, and 47% and 0.4% for tight b -tags. Events with at least one tight and one loose b -tag are classified as double-tagged (DT). Events not in the DT sample that contain a single tight b -tag are classified as single-tagged (ST). The dijet $H \rightarrow b\bar{b}$ candidate is composed of the two highest p_T tagged jets in DT events, and the tagged jet plus the highest p_T non-tagged jet in ST events.

IV. SIGNAL AND BACKGROUND ESTIMATION

The dominant background process is the production of a Z boson in association with jets, with the Z decaying to dileptons (Z +jets). The light-flavor component (Z +LF) includes jets from only light quarks (uds) or gluons. The heavy-flavor component (Z +HF) includes non-resonant $Z + b\bar{b}$ which has the same final state as the signal,

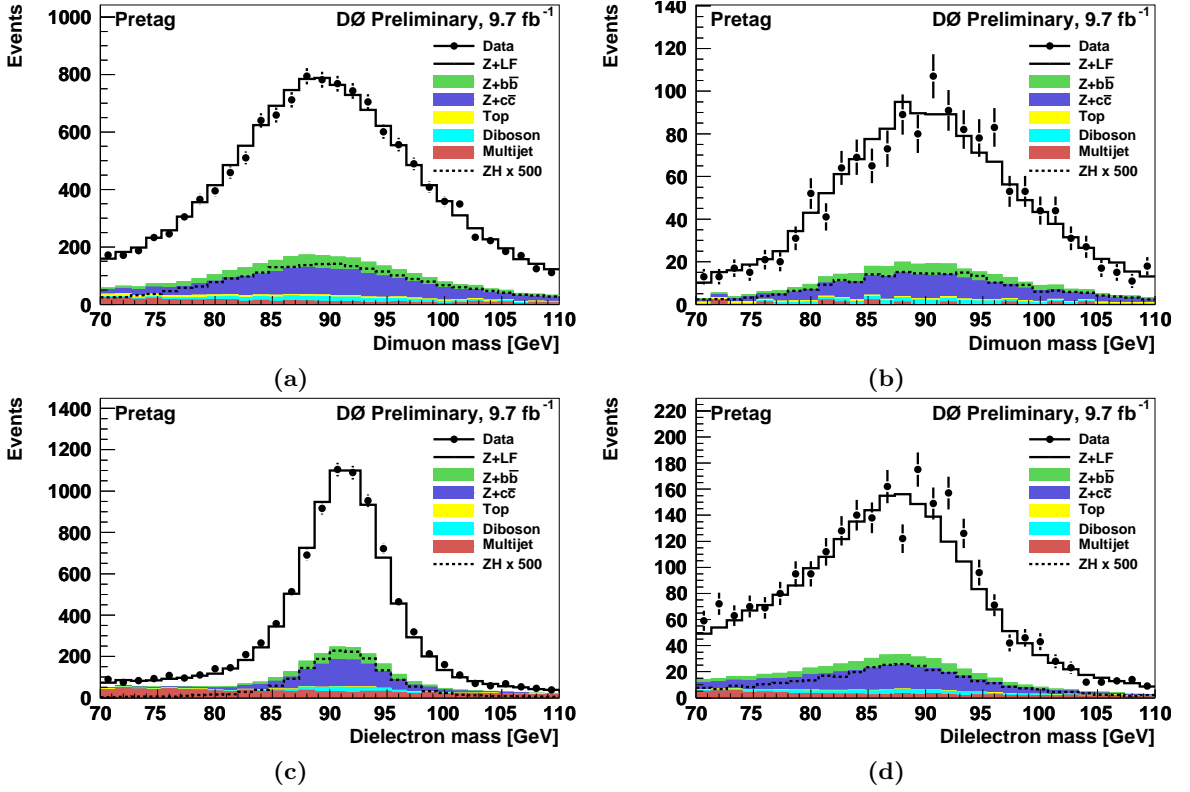


FIG. 1: The dilepton mass spectra in the (a) $\mu\mu$, (b) $\mu\mu_{\text{trk}}$, (c) ee and (d) ee_{ICR} channels. Distributions are shown in the “pretag” control sample, in which all selection requirements except b -tagging are applied. Signal distributions, for $M_H = 125$ GeV, are scaled by a factor of 500.

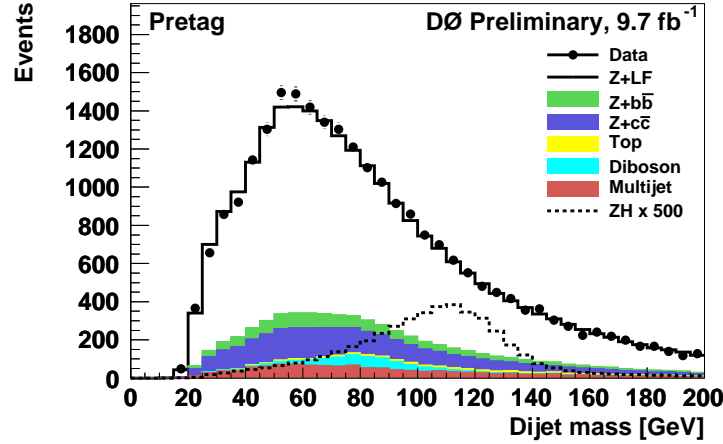


FIG. 2: Distribution of the dijet invariant mass in the combined ee , ee_{ICR} , $\mu\mu$ and $\mu\mu_{\text{trk}}$ sample after requiring two leptons and at least two jets (pretag). The signal distribution ($M_H = 125$ GeV) is scaled by a factor of 500.

and non-resonant $Z + c\bar{c}$ production. The remaining backgrounds are from $t\bar{t}$ and diboson production, and from multijet events with non-prompt muons or with jets misidentified as electrons. We simulate ZH and inclusive diboson production with PYTHIA [13]. In the ZH samples, we consider the contributions to the signal from the $\ell^+\ell^-b\bar{b}$, $\ell^+\ell^-c\bar{c}$, and $\ell^+\ell^-\tau^+\tau^-$ final states. The Z +jets and $t\bar{t} \rightarrow \ell^+\nu b\ell^-\bar{\nu}b$ processes are simulated with ALPGEN [14], followed by PYTHIA for parton showering and hadronization. All simulated samples are generated using the CTEQ6L1 [15] leading-order parton distribution functions (PDF).

The events generated with ALPGEN use PYTHIA for parton showering and hadronization. Because this procedure

	Data	Total Background	Multijet	Z +LF	Z +HF	Diboson	$t\bar{t}$	ZH
inclusive	1845610	1841683	160746	1630391	46462	2914	1170	17
pretag	25849	25658	1284	19253	4305	530	285	9.1
ST	886	824	54	60	600	33	77	2.5
DT	373	366	25.7	3.5	219	19	99	2.9

TABLE I: Expected and observed event yields for all lepton channels combined after requiring two leptons (inclusive), after also requiring at least two jets (pretag), and after requiring exactly one (ST) or at least two (DT) b -tags. The ZH sample yields are for $M_H = 125$ GeV. Expected yields are obtained following the background normalization procedure described in Section IV.

Channel	ee	ee_{ICR}	$\mu\mu$	$\mu\mu_{\text{trk}}$
ST	1.26	0.14	0.89	0.20
DT	1.47	0.16	1.03	0.22

TABLE II: Signal yields in the ST and DT samples for each channel, assuming $M_H = 125$ GeV.

can generate additional jets, we use a matching procedure to avoid double counting partons produced by ALPGEN and those subsequently added by the showering in PYTHIA [16]. All samples are processed using a detector simulation program based on GEANT3 [17], and the same offline reconstruction algorithms used to process the data. Events from randomly chosen beam crossings are overlaid on the generated events to model the effect of multiple $p\bar{p}$ interactions and detector noise.

The cross section and branching ratio for signal are taken from Refs. [18, 19]. For the diboson processes, next-to-leading order (NLO) cross sections are used [20]. The $t\bar{t}$ cross section is scaled to approximate next-to-NLO [21], and the inclusive Z -boson cross section is scaled to next-to-NLO [22]. Additional NLO heavy-flavor corrections, calculated from MCFM, are applied to $Z + b\bar{b}$ and $Z + c\bar{c}$.

To improve the modeling of the p_T distribution of the Z boson, the simulated Z boson events are reweighted to be consistent with the observed dielectron p_T spectrum in data [23].

The energies of simulated jets are modified to reproduce the resolution and energy scale observed in data. Scale factors are applied to account for differences in reconstruction efficiency between the data and simulation. Additional corrections are applied to improve agreement between data and background simulation, using two control samples with negligible signal contributions: the inclusive sample and the pretag sample mentioned above. The $\mu\mu$, $\mu\mu_{\text{trk}}$ and ee_{ICR} distributions are corrected for trigger efficiencies. For the ee channel, no correction is applied as the combination of all triggers is nearly 100% efficient. Motivated by a comparison with the SHERPA generator [24], the Z +jets events are reweighted to improve the ALPGEN modeling of the distributions of the pseudorapidities of the two jets. In our signal samples, we correct the generator level p_T of the ZH system to match the distribution from RESBOS [25].

The multijet backgrounds are estimated from control samples in the data. In the dimuon ($\mu\mu$) channel, a multijet event must contain a Z candidate which passes all event selection requirements except isolation and fails the opposite sign requirement. In the muon-plus-track ($\mu\mu_{\text{trk}}$) channel, multijet events are defined as those which pass all selection criteria, except the two muons have same-sign charges. For the ee channel, the electrons must fail isolation and shower shape requirements. For the ee_{ICR} channel, the electron in the ICR must fail a requirement on the multivariate discriminant.

The normalizations of the multijet background and all simulated samples are adjusted by scale factors determined from a simultaneous fit to the $m_{\ell\ell}$ distributions in the 0 jet, 1 jet and ≥ 2 jet samples of each lepton selection. This improves the accuracy of the background model and reduces the impact of systematic uncertainties that affect pretag event yields (e.g., uncertainties on luminosity and lepton identification). The region $40 < m_{\ell\ell} < 60$ GeV, where the multijet contribution is most prominent, is included in the fit to normalize the multijet control samples to the actual multijet contribution. The inclusive sample constrains the lepton trigger and identification efficiencies, while the pretag sample, which includes jet requirements, is used to correct the Z +jets cross section by a common scale factor $k_{Z+\text{jets}}$. We find that $k_{Z+\text{jets}}$ is within 7% of unity. The total event yields after applying all corrections and normalization factors are shown in Table I. The ST and DT signal yields for the individual channels are displayed in Table II.

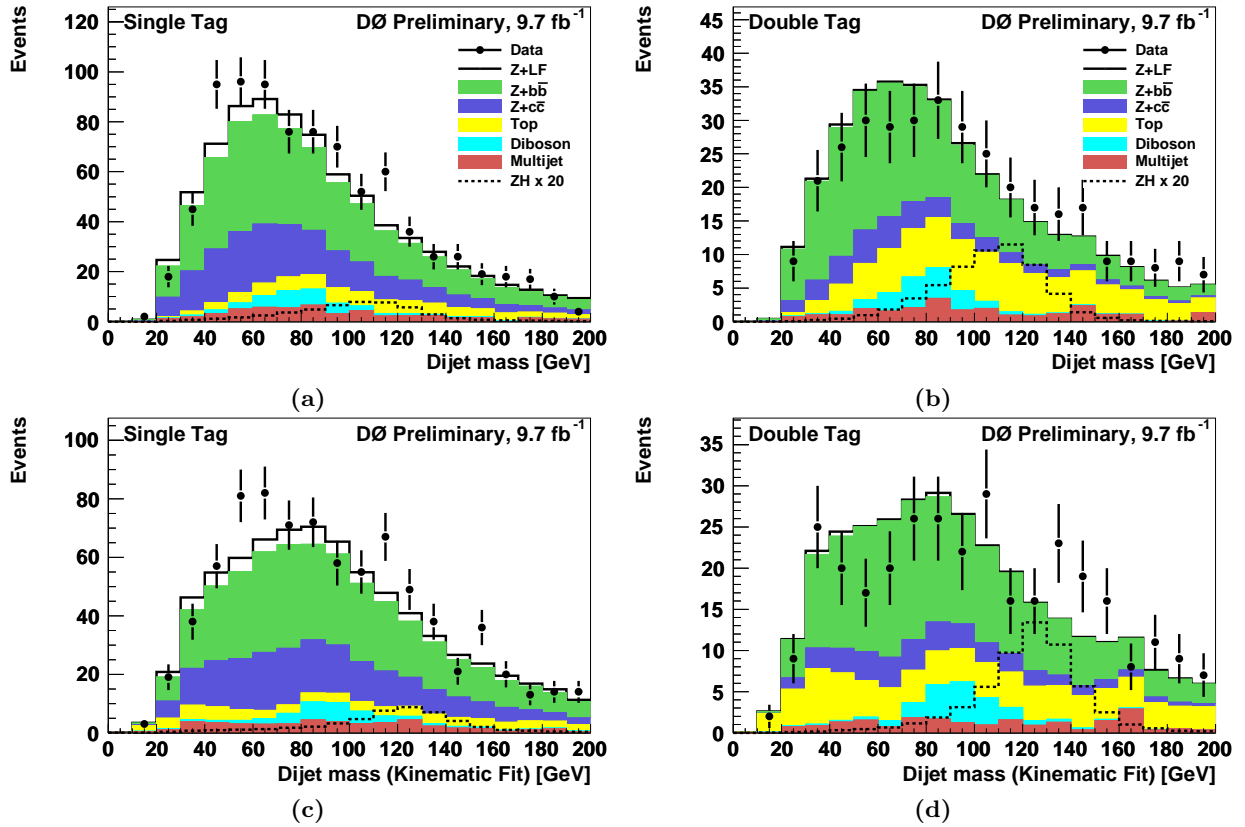


FIG. 3: Dijet invariant mass distributions before the kinematic fit in (a) ST events and (b) DT events; and after the kinematic fit in (c) ST events and (d) DT events, combined for all lepton channels. Signal distributions ($M_H = 125$ GeV) are shown with the SM cross section multiplied by 20.

V. MULTIVARIATE ANALYSIS

To exploit the fully constrained kinematics of the $ZH \rightarrow \ell^+\ell^-b\bar{b}$ process, the energies of the candidate leptons and jets are adjusted within their experimental resolutions with a likelihood fit that constrains $m_{\ell\ell}$ to the mass and width of the Z , and constrains the p_T of the $\ell^+\ell^-b\bar{b}$ system to zero, with an expected width determined from ZH MC events.

The kinematic fit improves the dijet mass resolution by 10–15%. Distributions of the dijet invariant mass spectra before and after adjustment by the kinematic fit, are shown in Figs. 3.

To improve the separation of signal from background using the most significant kinematic information, we use the TMVA software package [26] to develop a two step multivariate analysis strategy based on random forest (RF) discriminants. In the first step, we train a dedicated RF ($t\bar{t}$ RF) that takes $t\bar{t}$ as the only background and ZH as the signal. This approach takes advantage of the unique signature of the $t\bar{t}$ background, for instance the presence of large missing transverse energy, \cancel{E}_T . In the second step, we use the $t\bar{t}$ RF to define two independent regions: a $t\bar{t}$ enriched region ($t\bar{t}$ RF < 0.5) and a $t\bar{t}$ depleted region ($t\bar{t}$ RF \geq 0.5). In each region, we train a global RF to separate the signal from all backgrounds. In both steps we consider ST and DT events separately, and retrain the discriminants for each assumed value of M_H . Thus, we obtain a separate global RF in each of four regions for each value of M_H : for ST and DT events in the $t\bar{t}$ enriched and depleted regions.

Well-modeled kinematic variables are chosen as inputs for the analysis: the transverse momenta of the two b -jet candidates and the dijet mass, before and after the jet energies are adjusted by the kinematic fit; angular differences within and between the dijet and dilepton systems; the opening angle between the proton beam and the Z candidate in the rest frame of the Z boson [27]; and composite kinematic variables, such as the p_T of the dijet system and the scalar sum of the p_T values of the leptons and jets. A complete list of input variables is shown in Table III, and some sample input distributions are shown in Fig. 4.

Both the $t\bar{t}$ RFs and the global RFs are built from 500 decision trees. A separate set of RFs are trained for the ST and DT samples, and for each assumed value of M_H . Each tree uses a randomly chosen subset of the simulated

TABLE III: Variables used for the $t\bar{t}$ and global RF training. The jets that form the Higgs boson candidate are referred to as b_1 and b_2 .

variables	definition	$t\bar{t}$ RF	global RF
$m_{bb}(m_{bb}^{fit})$	invariant mass of the dijet system before (after) the kinematic fit	✓	✓
$p_T^{b1}(p_T^{b1,fit})$	transverse momentum of the first jet before (after) kinematic fit	✓	✓
$p_T^{b2}(p_T^{b2,fit})$	transverse momentum of the second jet before (after) kinematic fit	✓	✓
p_T^{bb}	transverse momentum of the dijet system before the kinematic fit	✓	✓
$\Delta\phi(b_1, b_2)$	$\Delta\phi$ between the two jets in the dijet system	—	✓
$\Delta\eta(b_1, b_2)$	$\Delta\eta$ between the two jets in the dijet system	—	✓
$m(\sum j_i)$	invariant mass of all jets in the event (the multijet mass)	✓	✓
$p_T(\sum j_i)$	transverse momentum of all jets in the event	✓	✓
$H_T(\sum j_i)$	scalar sum of the transverse momenta of all jets in the event	✓	—
$p_T^{bb}/(p_T^{b1} + p_T^{b2})$	ratio of dijet system p_T over the scalar sum of the p_T of the two jets	✓	—
$m_{\ell\ell}$	invariant mass of the dilepton system	✓	—
$p_T^{\ell\ell}$	transverse momentum of the dilepton system	✓	✓
$\Delta\phi(\ell_1, \ell_2)$	$\Delta\phi$ between the two leptons	✓	✓
$\text{colinearity}(\ell_1, \ell_2)$	cosine of the angle between the two leptons (colinearity)	✓	✓
$\Delta\phi(\ell\ell, bb)$	$\Delta\phi$ between the dilepton and dijet systems	✓	✓
$\cos\theta^*$	cosine of the angle between the incoming proton and the Z in the zero momentum frame [27]	—	✓
$m(\ell\ell bb)$	Invariant mass of dilepton plus dijet system	—	✓
$H_T(\ell\ell bb)$	Scalar sum of the transverse momenta of the leptons and jets	—	✓
\cancel{E}_T	missing transverse energy of the event	✓	—
\cancel{E}_T^{sig}	the \cancel{E}_T significance [28]	✓	✓
$-\ln L_{fit}$	negative log likelihood from the kinematic fit	✓	✓
$t\bar{t}$ RF	$t\bar{t}$ RF output	—	✓

signal and background events. At each decision of each tree, a subset of nine of the inputs is randomly chosen for consideration. The RF output is the average of the output from each decision tree. Comparisons of the data and MC distributions of the $t\bar{t}$ RF output summed over all lepton channels are shown for $M_H = 125$ GeV in Figure 5. The $t\bar{t}$ depleted region contains 94% (93%) of the DT (ST) signal contribution and 55% (82%) of DT (ST) background events. The global RF outputs for all lepton channels combined are shown for pretag events in Fig. 6. The global RF outputs are displayed separately for ST and DT events in the $t\bar{t}$ depleted and enriched regions in Fig. 7. Post-kinematic fit dijet mass distributions for ST and DT in the $t\bar{t}$ depleted region are shown in Fig. 8.

VI. SYSTEMATIC UNCERTAINTIES

Systematic uncertainties resulting from the background normalization are assessed for the multijet contribution (typically 10% depending on the channel) and from uncertainties on lepton efficiency effects (4%). The normalization of the Z +jets sample to match the pretag data constrains that sample to the statistical uncertainty of the pretag data (<1%). However, the normalizations of the $t\bar{t}$, diboson, and ZH samples are sensitive to the ratios of these processes' cross sections to the Z cross section, for which we assign an uncertainty of 6%. The normalization to the pretag data, which is dominated by Z +LF, does not strongly constrain the cross sections of other processes. For Z +HF, a cross section uncertainty of 20% is determined from Ref. [20]. For other backgrounds, the uncertainties are 6%–10% [20, 21]. For the signal, the cross section uncertainty is 6% [18]. The normalization procedure described in Section IV reduces the impact of many of the remaining systematic uncertainties on the background size (except those related to b -tagging), but changes to the shape of the RF output distribution persist and are accounted for. Additional sources of systematic uncertainty include: jet energy scale, jet energy resolution, jet identification efficiency, b -tagging and trigger efficiencies, PDF uncertainties [29], data-determined corrections to the model for Z +jets, and modeling of the underlying event. The uncertainties from the factorization and renormalization scales in the simulation of Z +jets are estimated by scaling these parameters by factors of 0.5 and 2.

VII. HIGGS SEARCH RESULTS

We set 95% CL upper limits on the ZH cross section times branching ratio for $H \rightarrow b\bar{b}$ with a modified frequentist (CLs) method that uses the log likelihood ratio (LLR) of the signal+background (S+B) hypothesis to the background-

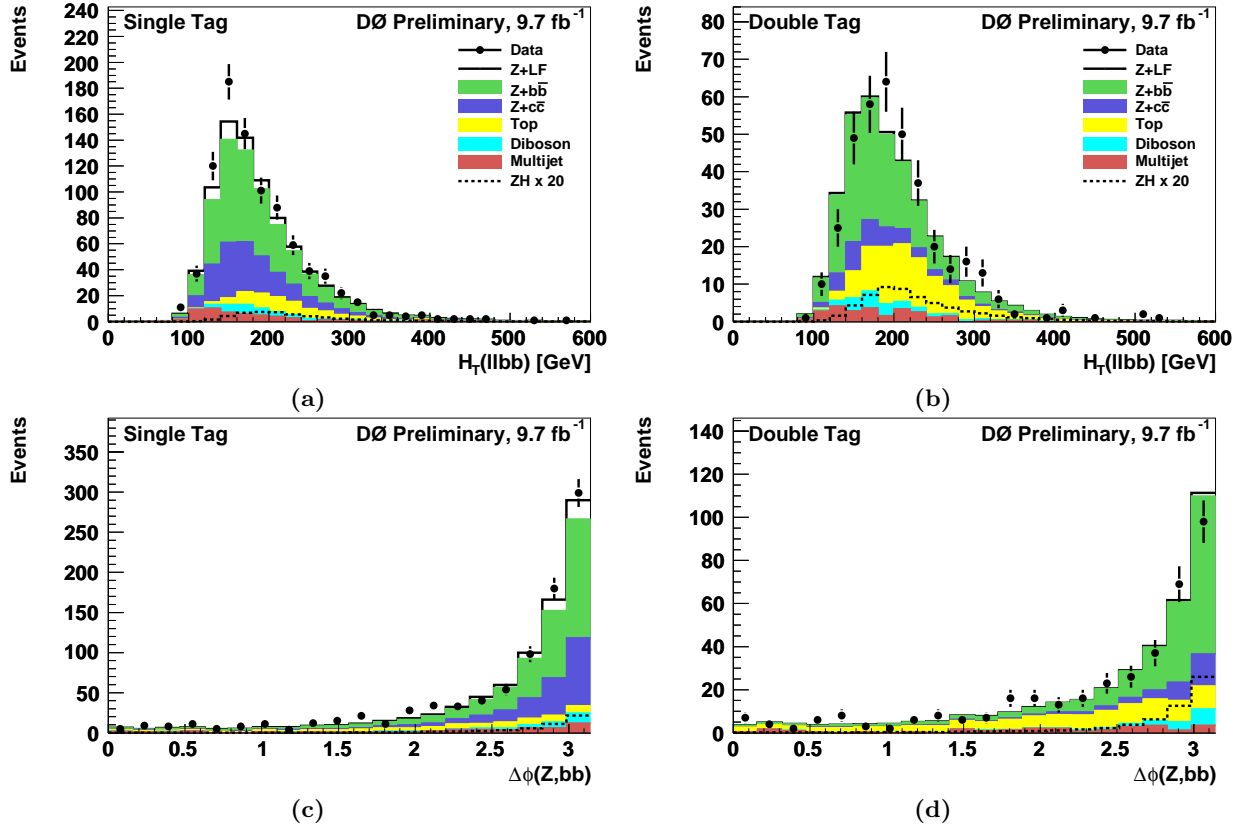


FIG. 4: $H_T(\ell\ell bb)$ distributions in (a) ST events and (b) DT events, and $\Delta\phi(\ell\ell, bb)$ distributions in (c) ST events and (d) DT events, combined for all lepton channels. Signal distributions ($M_H = 125$ GeV) are shown with the SM cross section multiplied by 20.

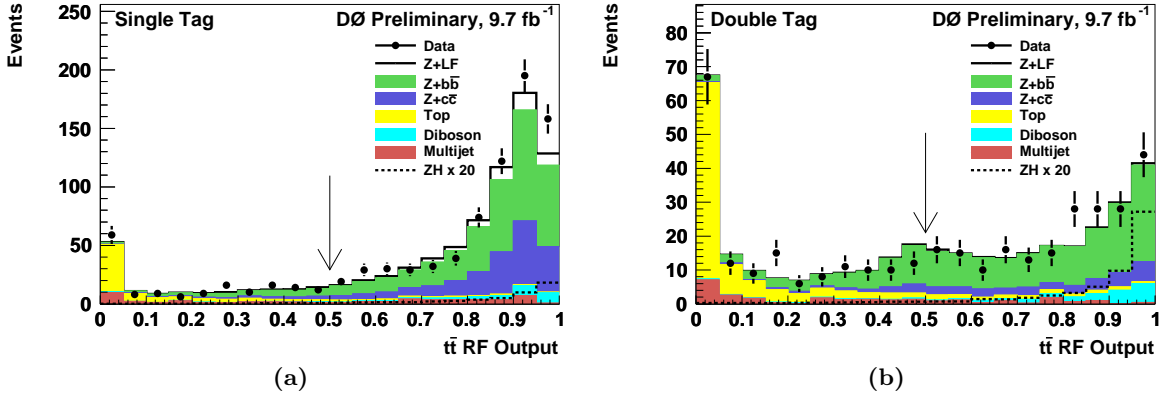


FIG. 5: The $t\bar{t}$ RF output ($M_H = 125$ GeV) for all lepton channels combined (a) ST and (b) DT events. Signal distributions are shown with the SM cross section multiplied by 20. The vertical arrows indicate the cut at $t\bar{t}$ RF = 0.5 which defines the $t\bar{t}$ enriched and depleted regions.

only (B) hypothesis [30]. We use as final discriminant variables the global RF outputs of the four samples (ST and DT in the $t\bar{t}$ depleted and $t\bar{t}$ enriched regions) in each channel along with the corresponding systematic uncertainties. To take advantage of the sensitivity in the more discriminating channels, we provide separate distributions for each channel to the limit-setting program.

To minimize the effect of systematic uncertainties, the likelihoods of the B and S+B hypotheses are maximized by independent fits which vary nuisance parameters that model the systematic uncertainties [31]. The correlations among systematic uncertainties are maintained across channels, backgrounds and signal, as appropriate. The RF distribution

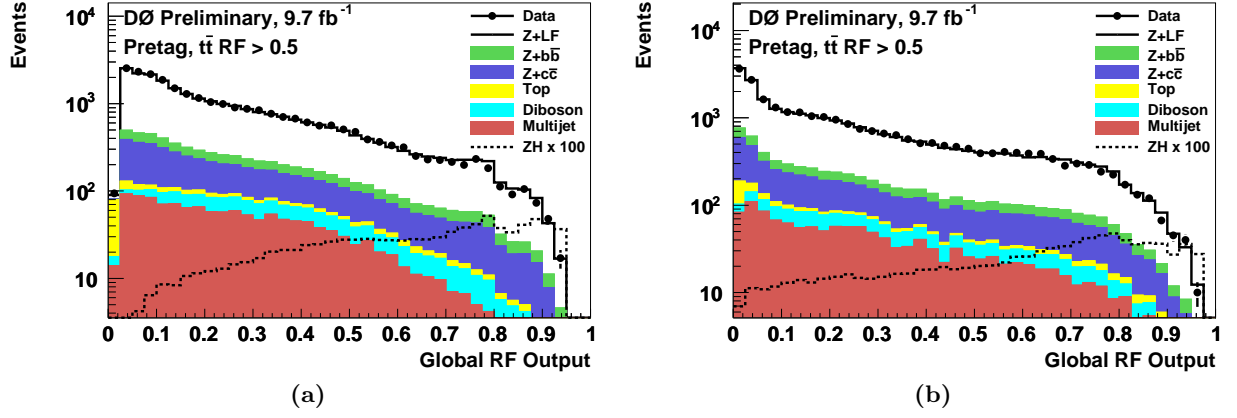


FIG. 6: Global RF output distributions in the $t\bar{t}$ depleted region for all lepton channels combined assuming $M_H = 125$ GeV for (a) pretag events evaluated with the ST-trained RF and (b) pretag events evaluated with the DT-trained RF. Signal distributions are shown with the SM cross section multiplied by 100.

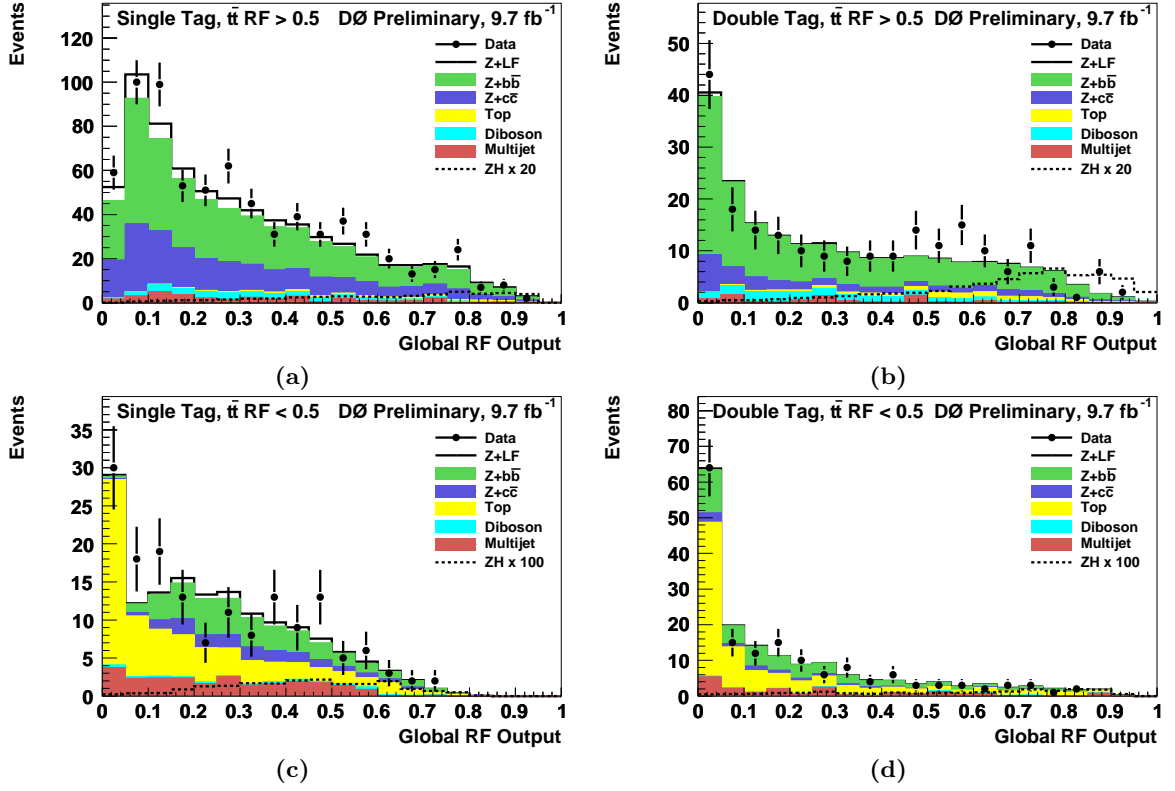


FIG. 7: Global RF output ($M_H = 125$ GeV) for all lepton channels combined in (a) ST and (b) DT events for the $t\bar{t}$ depleted-region and in (c) ST and (d) DT events for the $t\bar{t}$ enriched-region. Signal distributions are shown with the SM cross section multiplied by 20 for (a) and (b) and by 100 for (c) and (d).

after the background-only fit (post-fit), combined for all channels, is shown in Fig. 9 for ST and DT events separately in the $t\bar{t}$ depleted region. Also shown are the post-fit background subtracted RF distributions. Fig. 10 displays the same distributions in the $t\bar{t}$ enriched region.

Fig. 11 shows the observed LLR as a function of Higgs boson mass. Also shown are the expected (median) LLRs for the background-only and signal+background hypotheses, together with the one and two standard deviation bands about the background-only expectation. The upper limits on the ZH cross section times branching ratio for $H \rightarrow b\bar{b}$, expressed as a ratio to the SM prediction, are presented as a function of M_H in Table IV and Fig. 12. At $M_H = 125$ GeV, the observed (expected) limit on this ratio is 7.1 (5.1).

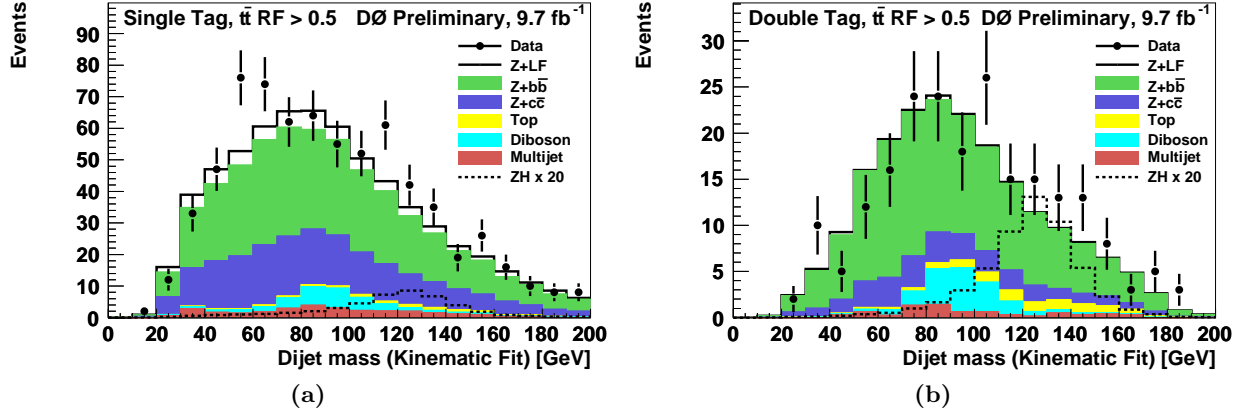


FIG. 8: Post-kinematic fit dijet mass distributions in the $t\bar{t}$ depleted region for all lepton channels combined assuming $M_H = 125$ GeV for (a) ST events and (b) DT events. Signal distributions are shown with the SM cross section multiplied by 20.

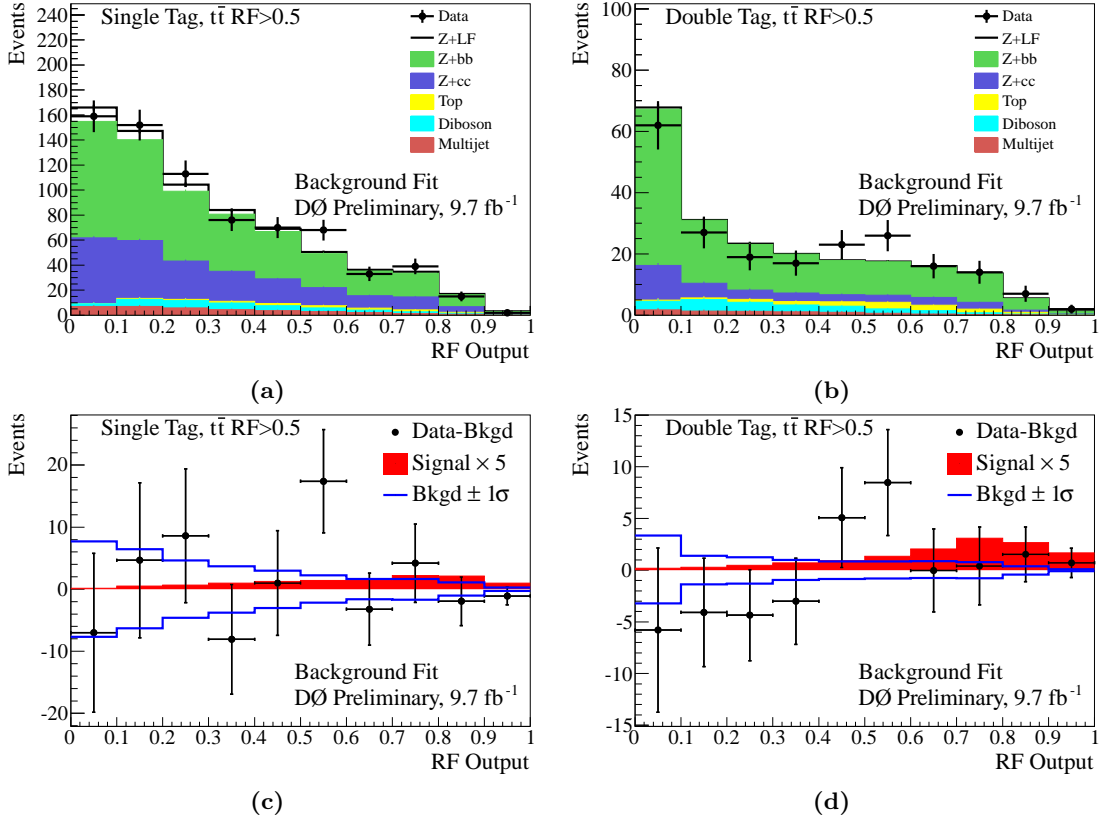


FIG. 9: Post-fit RF output distributions in the $t\bar{t}$ depleted region, assuming $M_H = 125$ GeV, after the fit to the background-only model for (a) ST events and (b) DT events. Background-subtracted distributions for (a) and (b) are shown in (c) and (d), respectively. Signal distributions are shown with the SM cross section scaled to $5 \times$ SM prediction in (c) and (d). The blue lines indicate the uncertainty from the fit.

TABLE IV: The expected and observed 95% C.L. upper limits on the SM Higgs boson production cross section times branching ratio for $ZH \rightarrow \ell^+ \ell^- b\bar{b}$, expressed as a ratio to the SM prediction.

M_H (GeV)	90	95	100	105	110	115	120	125	130	135	140	145	150
Expected	2.6	2.7	2.8	3.0	3.4	3.7	4.3	5.1	6.6	8.7	12	18	29
Observed	1.8	2.3	2.2	3.0	3.7	4.3	6.2	7.1	12	16	19	31	53

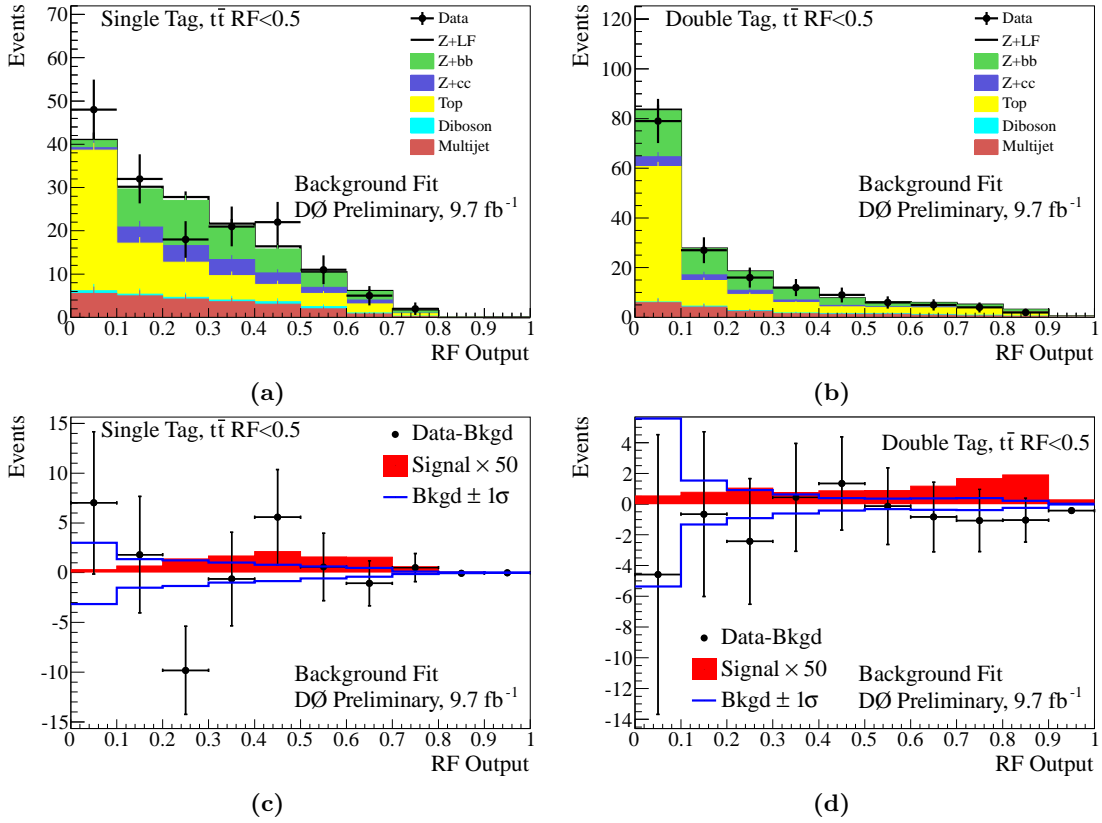


FIG. 10: Post-fit RF output distributions in the $t\bar{t}$ enriched region, assuming $M_H = 125$ GeV, after the fit to the background-only model for (a) ST events and (b) DT events. Background-subtracted distributions for (a) and (b) are shown in (c) and (d), respectively. Signal distributions are shown with the SM cross section scaled to $50 \times$ SM prediction in (c) and (d). The blue lines indicate the uncertainty from the fit.

In Appendix A we provide comparisons of these results to those obtained in Ref. [9]. We find that 78% of DT events and 73% of ST events with $t\bar{t}$ RF > 0.5 and global RF > 0.5 satisfied the requirement of global RF > 0.5 in Ref. [9]. The expected limits have improved by 10-15% depending on the assumed value of M_H .

VIII. SUMMARY

In summary, we have searched for SM Higgs production in association with a Z boson in the final state of two charged leptons (electron or muon) and two b -quark jets using a 9.7 fb^{-1} data set. We set upper limits on the ZH production cross section times branching ratio for $H \rightarrow b\bar{b}$. The observed (expected) limit for $M_H = 115$ GeV is a factor of 4.3 (3.7) larger than the SM prediction. At $M_H = 125$ GeV it is a factor of 7.1 (5.1) larger than the SM prediction.

Acknowledgments

We thank the staffs at Fermilab and collaborating institutions, and acknowledge support from the DOE and NSF (USA); CEA and CNRS/IN2P3 (France); FASI, Rosatom and RFBR (Russia); CNPq, FAPERJ, FAPESP and FUNDUNESP (Brazil); DAE and DST (India); Colciencias (Colombia); CONACyT (Mexico); KRF and KOSEF (Korea); CONICET and UBACyT (Argentina); FOM (The Netherlands); STFC and the Royal Society (United Kingdom); MSMT and GACR (Czech Republic); CRC Program and NSERC (Canada); BMBF and DFG (Germany); SFI (Ireland); The Swedish Research Council (Sweden); and CAS and CNSF (China).

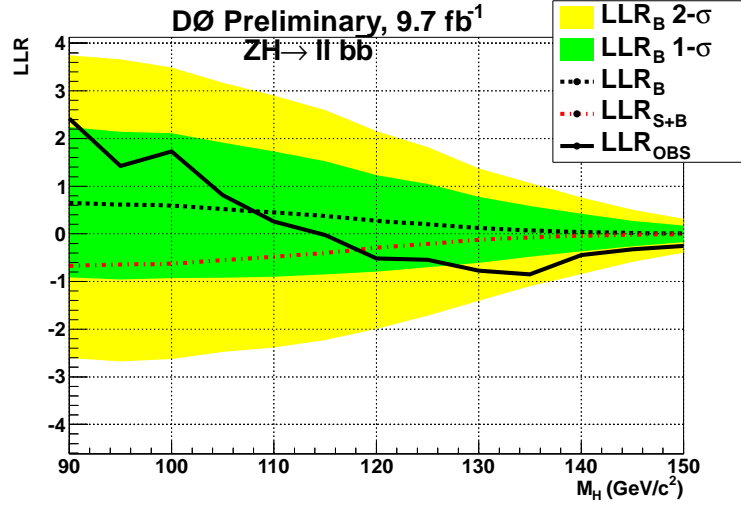


FIG. 11: Observed LLR as a function of Higgs boson mass. Also shown are the expected LLRs for the background-only (B) and signal+background (S+B) hypotheses, together with the one and two σ bands about the background-only expectation.

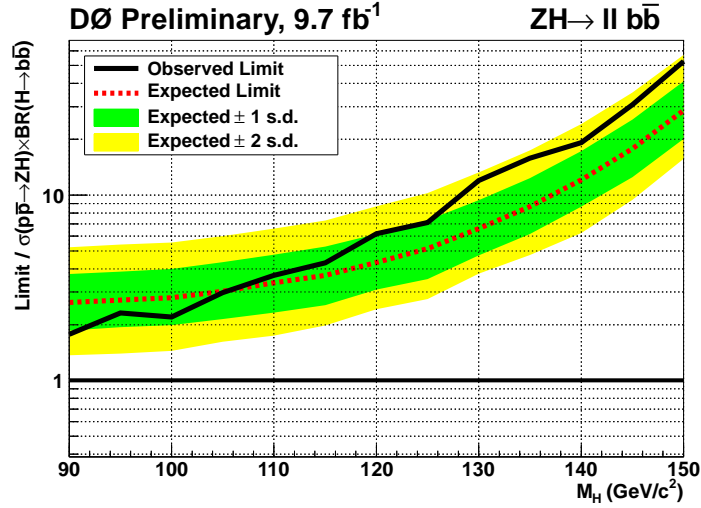


FIG. 12: Expected and observed 95% C.L. cross section upper limits on the ZH cross section time branching ratio for $H \rightarrow b\bar{b}$, expressed as a ratio to the SM prediction.

-
- [1] ALEPH, DELPHI, L3, and OPAL Collaborations, The LEP Working Group for Higgs Boson Searches, *Phys. Lett. B* **565**, 61 (2003).
 - [2] LEP Electroweak Working Group
<http://lepewwg.web.cern.ch/LEPEWWG/>
 - [3] Tevatron New Phenomena and Higgs Working Group
arXiv:1203.3774v1
 - [4] S. Chatrchyan *et al.* (CMS Collaboration), *Phys. Lett. B* **710**, 26 (2012).
 - [5] G. Aad *et al.* (ATLAS Collaboration) *Phys. Lett. B* **710**, 49 (2012).
 - [6] V.M. Abazov *et al.* (D0 Collaboration), DØ Note 6340-CONF (2012)
V.M. Abazov *et al.* (D0 Collaboration), *Phys. Rev. Lett.* **104**, 071801 (2010).
 - [7] V. M. Abazov *et al.* (D0 Collaboration), *Nucl. Instrum. Methods Phys. Res. Sect. A* **565**, 463 (2006).
 - [8] M. Abolins *et al.*, *Nucl. Instrum. Methods Phys. Res. Sect. A* **584**, 75 (2008); R. Angstadt *et al.*, *Nucl. Instrum. Methods Phys. Res. Sect. A* **622**, 298 (2010).
 - [9] V.M. Abazov *et al.* (D0 Collaboration), DØ Note 6296-CONF (2012).
 - [10] Pseudorapidity is defined as $\eta = -\ln[\tan(\theta/2)]$, where θ is the polar angle of a vector relative to the proton beam direction. ϕ is defined to be the azimuthal angle in the plane transverse to the proton beam direction. The pseudorapidity of a vector which passes through the detector center being at the nominal proton-antiproton collision point is denoted by η_{det} .
 - [11] G. C. Blazey *et al.*, arXiv:hep-ex/0005012 (2000).
 - [12] V. M. Abazov *et al.* (D0 Collaboration), *Nucl. Instrum. Methods in Phys. Res. Sect. A* **620**, 490 (2010).
 - [13] T. Sjöstrand *et al.*, *Comput. Phys. Commun.* **135**, 238 (2001). Version 6.409 was used.
 - [14] M. L. Mangano *et al.*, *J. High Energy Phys.* **0307**, 001 (2003). Version 2.11 was used.
 - [15] J. Pumplin *et al.*, *J. High Energy Phys.* **07**, 012 (2002).
 - [16] S. Höche *et al.*, arXiv:hep-ph/0602031 (2006).
 - [17] R. Brun, F. Carminati, CERN Program Library Long Writeup W5013 (1993).
 - [18] J. Baglio and A. Djouadi, arXiv:1003.4266v2 [hep-ph].
 - [19] S. Dittmaier *et al.* [LHC Higgs Cross Section Working Group], arXiv:1101.0593v2 (2011).
 - [20] J. Campbell and R.K. Ellis, <http://mcfm.fnal.gov/>.
 - [21] U. Langenfeld, S. Moch, and P. Uwer, *Phys. Rev. D* **80**, 054009 (2009).
 - [22] R. Hamberg, W.L. van Neerven and W.B. Kilgore, *Nucl. Phys. B* **359**, 343 (1991), [*Erratum ibid. B* **644**, 403 (2002)].
 - [23] V. M. Abazov *et al.* (D0 Collaboration), *Phys. Rev. Lett.* **100**, 102002 (2008).
 - [24] T. Gleisberg *et al.*, *J. High Energy Phys.* 02 (2004) 056; J. Alwall *et al.*, *Eur. Phys. J. C* **53**, 473 (2008).
 - [25] C. Balazs and C.-P. Yuan, *Phys.Rev.D* 56:5558-5583,1997.
 - [26] A. Hoecker *et al.*, arXiv:physics/0703039v5 [physics.data-an] version 4.1.0.
 - [27] S. Parke and S. Veseli, *Phys. Rev. D* **60**, 093003 (1999).
 - [28] A. Schwartzman, Report No. FERMILAB-THESIS-2004-21.
 - [29] D. Stump *et al.*, *J. High Energy Phys.* **10**, 046 (2003).
 - [30] T. Junk, *Nucl. Instrum. Methods Phys. Res., Sect. A* **434**, 435 (1999); A. Read, *J. Phys. G* **28** 2693 (2002).
 - [31] W. Fisher, FERMILAB-TM-2386-E (2007).

APPENDIX A: COMPARISON WITH PREVIOUS RESULTS

In this appendix we document the comparison of these results with the most recent previous version of this analysis [9]. The expected limits are compared in Fig. 13a, and the observed limits are compared in Fig 13b. The expected limits have improved by 10-15%, depending on the assumed value of M_H . For $M_H \geq 120$ GeV there is no significant change in the observed limits, whereas at lower values of M_H the observed limits have become somewhat less stringent. To visualize the sensitivity of the combined $ZH \rightarrow \ell\ell b\bar{b}$ analysis, it is useful to collect all of the analyzed subsamples into a single distribution. To preserve the sensitivity from the bins with high signal-to-background ratios (s/b), only bins with similar s/b are combined. The aggregate distribution is then constructed by re-ordering the bins from the input distributions according to s/b . Because the range of s/b is large, the variable $\log(s/b)$ is used. The resulting distributions from Ref. [9] and from this analysis are shown in Fig. 14. In this analysis, the distribution ranges to larger values of $\log(s/b)$ than in the previous analysis, indicating an increase in sensitivity. Fig. 15 shows the same distributions after subtraction of the background. Integrating the distributions in Fig. 14 from *right to left* (i.e. starting from the highest s/b events) allows one to see how the data compare to the background-only and signal+background hypotheses as the most significant events are accumulated. Fig. 16 shows these cumulative distributions for the ≈ 150 most significant events as a function of the integrated number of predicted signal events. In this result, the highest s/b bins contain a small excess of signal-like candidate events.

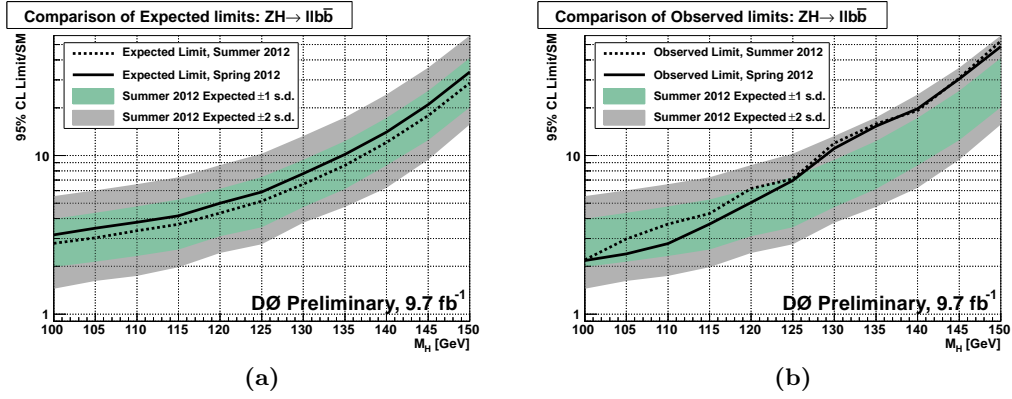


FIG. 13: Comparison of (a) expected, and (b) observed limits for this result, and the result from Ref. [9].

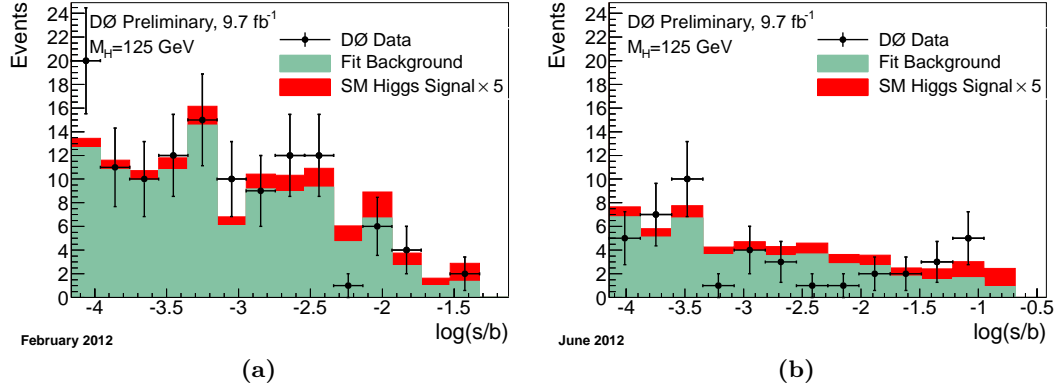


FIG. 14: Distributions of $\log(s/b)$ from (a) the results in Ref. [9] and from (b) this analysis for a Higgs boson mass of 125 GeV. The signal has been scaled by a factor of five. The data are shown with points and the expected signal is stacked on top of the sum of backgrounds.

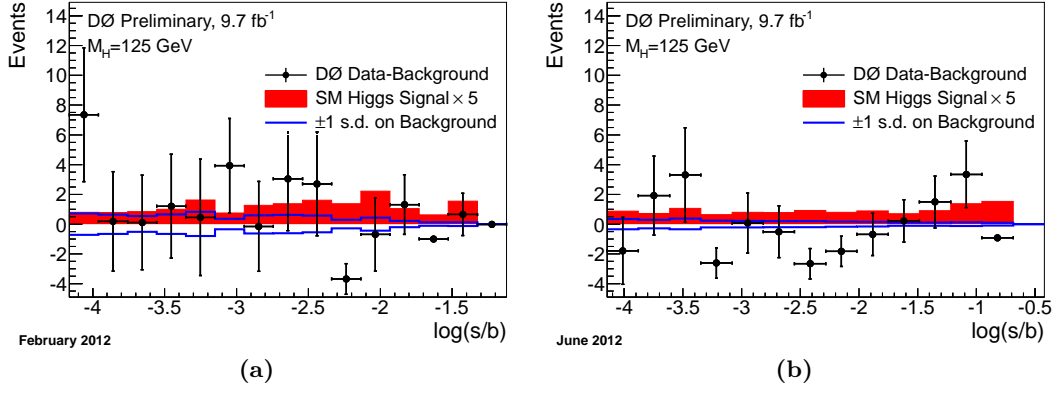


FIG. 15: Background subtracted distributions of the data $\log(s/b)$ for (a) the results in Ref. [9] and (b) in this analysis for a Higgs boson mass of 125 GeV. The background subtracted data are shown as points and the signal, scaled by a factor of five is shown as the red histograms. The blue lines indicate the uncertainty on the background prediction.

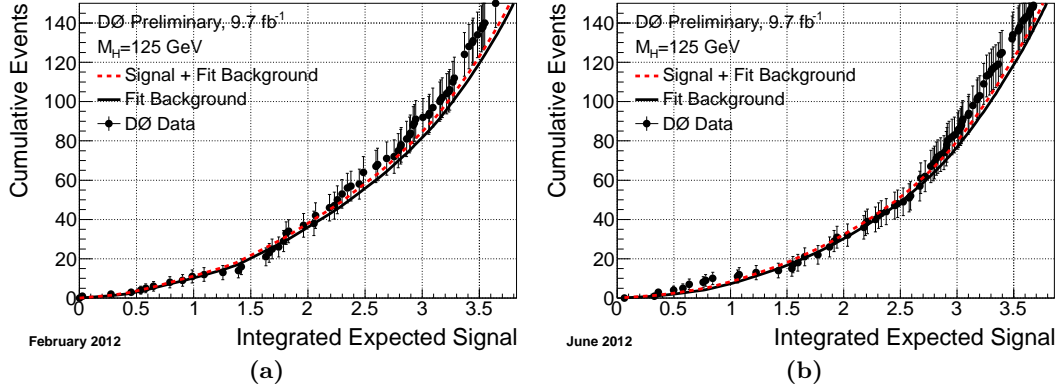


FIG. 16: Cumulative number of events for the highest s/b bins for $M_H = 125$ GeV for (a) the results in Ref. [9] and (b) in this analysis. The integrated background-only and signal+background predictions are shown as a function of the accumulated number of signal events. The points show the integrated number of observed events.